


# Enhancement of structural and electrical properties of novelty nanoferrite materials

Asmaa A. H. El-Bassuony<sup>1</sup> 

Received: 12 April 2017 / Accepted: 6 June 2017 / Published online: 14 June 2017  
© Springer Science+Business Media, LLC 2017

**Abstract** Novelty Cu–Cr nanoferrite, with the general formula  $\text{CuCr}_{0.3}\text{R}_{0.03}\text{Fe}_{1.67}\text{O}_4$  (where R=Sm, Nd, Ce and La), were prepared by standard ceramic method and characterized by X-ray diffraction (XRD) analysis. Field emission scanning electron microscope (FESEM) and Energy dispersive X-ray analysis (EDX) were obtained for all samples. The effect of doping Cu–Cr ferrite with different rare earth ( $\text{R}^{3+}$ ) types on the structural and electrical properties showed that the ionic radius, electronic configuration and ionization potential for different  $\text{R}^{3+}$  could explain the results. Introducing  $\text{R}^{3+}$  in Cu–Cr ferrite retained parent cubic spinel structure ferrite. All  $\text{R}^{3+}$  types induced cation redistribution. At low temperature the ionic radius of  $\text{R}^{3+}$  control the conduction, whereas at high temperature the ionization potential have the decisive effect. It was found that La-doped Cu Cr sample had the lowest AC conductivity due to its large ionic radius and high ionization potential promising application in memories and microelectronics.

## 1 Introduction

Ferrites are group of magnetic oxides containing iron as a major metallic element. Many properties of ferrites are drastically influenced by the type of distribution cations in either A- and B-sublattices. Their properties are very sensitive to the method of preparation [1]. Mixed copper ferrites have been commercially used for many years

as high-frequency devices such as radio frequency coils, transformer cores, rod antennas and magnetic cores of read-write heads for high speed digital tapes [2]. Therefore, to meet the demands of applications at microwave frequencies, attempts are taken to develop these ferrites. For this purpose two major possibilities are available, controlling the sintering temperature, atmosphere or adding some additives or substituents as R ions into Cu–Cr ferrite lattice. It is known that rare-earth (R) atoms play an important role in electrical properties as reported [3]. The electrical conductivity and dielectric behavior of ferrites markedly depend on the preparation condition such as a sintering temperature, chemical composition, the quantity and type of substitutions [4]. The influence of these factors on the electrical properties have much valuable information on the behavior of the delocalized electric charge carriers which can lead to understand of the mechanism of electric conduction and the dielectric in ferrite systems.

The main purpose of this work is to enhance the structural and electrical properties of Cu–Cr nanoferrite using different rare earth ions. Also, there is shortage in literature in the investigation materials which are important in many technological applications.

## 2 Experimental work

Doped materials were prepared using standard ceramic technique [5]. Ferrites of the general formula  $\text{CuCr}_{0.3}\text{R}_{0.03}\text{Fe}_{1.67}\text{O}_4$  (where R=Sm, Nd, Ce and La) have initial ingredients copper II oxide, chromium III oxide, samarium III oxide, neodymium III oxide, cerium III oxide, lanthanum III oxide and iron III oxide. The mixtures were grinded for 3 h, then they were compressed to pellets. The samples were fired using Lenton furnace UAF

✉ Asmaa A. H. El-Bassuony  
asmaa@sci.cu.edu.eg  
<http://scholar.cu.edu.eg/?q=phys/>

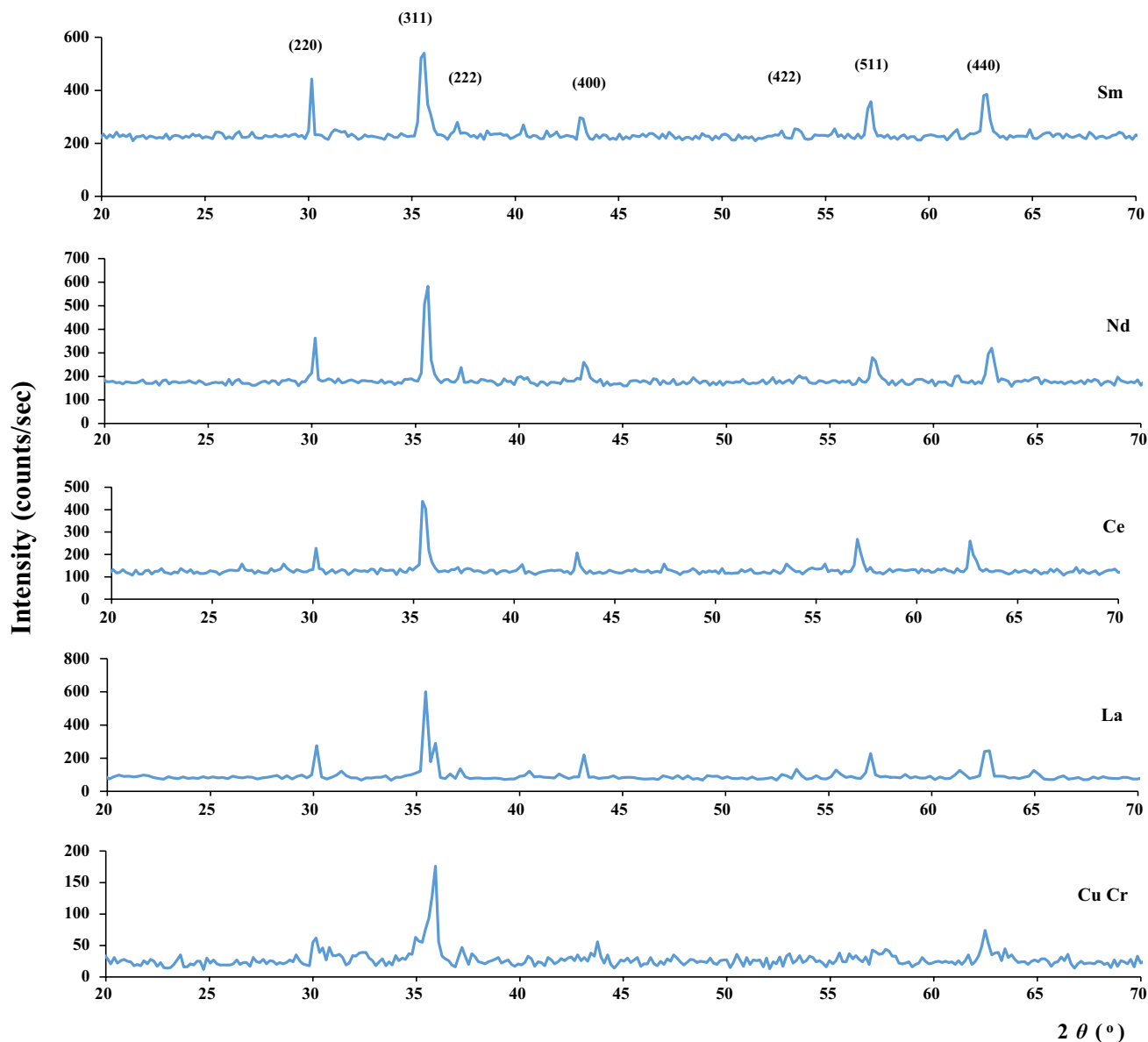
<sup>1</sup> Physics Department, Faculty of Science, Cairo University, Giza, Egypt

16/5 (England) with microprocessor to control both the rates of heating and cooling runs. Presintering was carried out at 800 °C for 6 h with heating rate of 4 °C/min. Then, final sintering was carried out at 1000 °C for 8 h with heating rate 4 °C/min. The samples were annealed at 1000 °C and all analyses have done at this annealed temperature. The X-ray diffraction patterns were obtained using Diano corporation of target Cu–K $\alpha$  ( $\lambda = 1.5424 \text{ \AA}$ ). The average crystallite size was calculated from the X-ray enlargement line ( $d_{311}$ ) calculated by Scherrer's equation considering the half height and the enlargement of the peaks of diffraction [6]. The morphology was analyzed by the Scanning Electron Microscopy for the samples using SEM Model Quanta 250 FEG (Field Emission Gun) attached with EDX

Unit (Energy Dispersive X-ray Analyses), with accelerating voltage 30 KV, magnification  $\times 14$  up to 1000000 and resolution for Gun.1n, FEI company, Netherlands. The electrical properties were measured by Hioki bridge Japan LCR Hi tester type 3530 (Japan) at frequencies ranging from 100 kHz to 5 MHz.

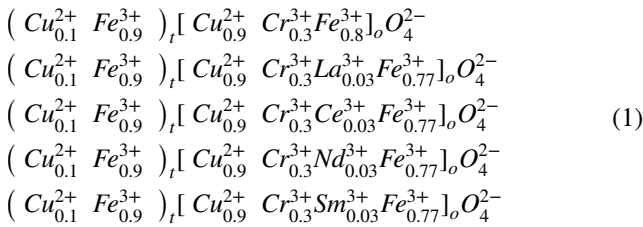
### 3 Result and discussion

Figure 1 showed XRD analysis for  $\text{CuCr}_{0.3}\text{R}_{0.03}\text{Fe}_{1.67}\text{O}_4$ , R=La, Ce, Nd and Sm. All samples showed single face spinel structure with small amount of secondary phase  $\text{R}_2\text{O}_3$ . These diffraction patterns were considered as face



**Fig. 1** X-ray diffractograms for different rare earth doped Cu–Cr ferrite

centered cubic (fcc) structure. Compared with ICDD card number 77-0013, it is found that the strong diffraction from the planes 311, 220, 400, 511 and 440 as well as weak diffraction from the planes 222 and 422 appeared in the X-ray diffractograms. La<sup>3+</sup> ion on Cu–Cr ferrite behaved differently compared with the other rare earth element (R) ions. This may be attributed to its empty f-orbital, while the other rare earth metals the diffraction lines are shifted to lower diffraction angle (θ) with increasing the ionic radii of R ions. This may attributed to cations distribution of the ions as follow:



It was reported [7] that the planes in XRD analysis 220, 400, 422 and 440 are very sensitive to cation distribution at both tetrahedral and octahedral sites. Any alteration in cation distribution caused a significant change in XRD intensity ratios. The calculations resulted from XRD analysis were listed in Table 1. The crystallite size was calculated from the characteristics of the (311) XRD peaks using Debye–Scherrer’s equation:

$$D = \frac{k\lambda}{\beta \cos \theta} \tag{2}$$

where λ is the wavelength of CuKα radiation (=1.54056 Å), shape factor k=0.9, β is the contribution to the XRD peak width, full width at half maximum (FWHM) due to the small size of crystallites in radians. It was observed that the crystallite size was in the range from 100 to 161.4 nm and increased by increasing the ionic radii of R-ions. The lattice parameter for the investigated cubic spinel system (where a=b=c) is calculated using the formula [8]. The

experimental lattice parameter changed monotonically with the type of R ion, which was attributed to the small difference in ionic radius of R ions and interchange in the cation distributions among A-site and B-site of the spinel lattice and increased in the order La<sup>3+</sup> > Ce<sup>3+</sup> > Nd<sup>3+</sup> > Sm<sup>3+</sup>. Also, the increase of lattice parameter with increasing ionic radius of R ions due to the formation of secondary phases on the surface of ferrite grains during sintering process [9]. The theoretically lattice parameter (a<sub>th</sub>) are calculated from the relation [10] as follow:

$$a_{th} = \frac{8}{3\sqrt{3}} [(r_A + R_o) + \sqrt{3}(r_B + R_o)] \tag{3}$$

where R<sub>o</sub> is the radius of the oxygen ion (0.138 nm) [11], r<sub>A</sub> and r<sub>B</sub> are the ionic radii of tetrahedral (A) and octahedral (B) sites respectively. From Table 1 it is shown that the theoretical lattice parameter values follow the same trend as the experimental lattice parameter values [12].

The X-ray density, D<sub>x</sub> and bulk density, D<sub>b</sub> were determined [13] for various R in CuCr<sub>0.3</sub>R<sub>0.03</sub>Fe<sub>1.67</sub>O<sub>4</sub> and listed in Table 1. The X-ray densities, D<sub>x</sub>, for all samples were increased monotonically, with the type of R ions, compared to that of undoped ferrite, which is consistent with the decrease in the lattice constant. The percentage porosity (P) of ferrite materials are calculated using the relation [14]

$$P = 1 - \frac{D_b}{D_x} \times 100\% \tag{4}$$

Table 1, correlates the ionic radii of the rare earth ions with the porosity factor. Generally, there is a lowering in the porosity started after Nd-doped samples due to substitution process, where the addition of rare earth ions acts as a sintering catalyst that helps in the development of densification at lower temperature.

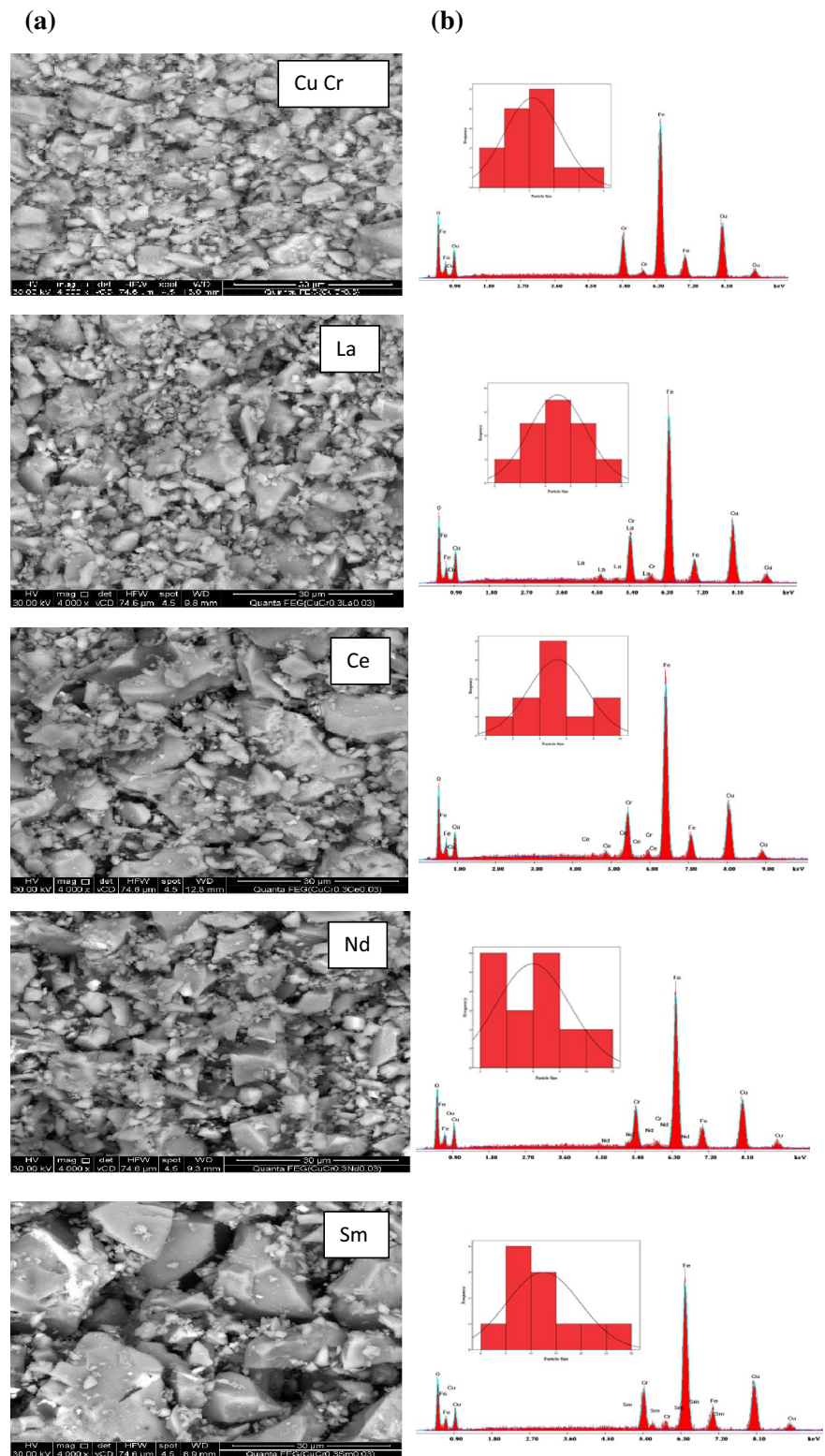
Tolerance factor T for spinel ferrite was suggested by the following relation [6]:

$$T = \frac{1}{\sqrt{3}} \left( \frac{r_A + R_o}{r_B + R_o} \right) + \frac{1}{\sqrt{2}} \left( \frac{R_o}{r_B + R_o} \right) \tag{5}$$

**Table 1** Values of ionic radius, crystallite size, experimental lattice parameter a<sub>exp</sub>, theoretical lattice parameter a<sub>th</sub>, X-ray density D<sub>x</sub>, bulk density D<sub>b</sub>, Porosity (P) and tolerance factor (T) of Cu–Cr–R ferrite

Sample	Ionic radius (Å)	Crystallite size (nm)	a <sub>exp</sub> (Å)	a <sub>th</sub> (Å)	D <sub>x</sub> (gm/cm <sup>3</sup> )	D <sub>b</sub> (gm/cm <sup>3</sup> )	P %	T
CuCr	–	100	8.363	8.382	5.406	4.573	15	1.0006
La	1.032	161.4	8.377	8.397	5.456	4.670	14	0.9978
Ce	1.010	108.8	8.375	8.396	5.440	3.953	27	0.9980
Nd	0.983	108.4	8.371	8.395	5.451	4.080	25	0.9982
Sm	0.958	104.3	8.370	8.394	5.457	4.279	22	0.9984

**Fig. 2** **a** The micrograph of FESEM of Cu–Cr–R ferrite. **b** EDX pattern for Cu–Cr–R ferrite. (The *inset* is the Histogram of the average particle size)



where  $r_A$ ,  $r_B$  and  $R_o$  are ionic radius of A-site, B-site and for oxygen ( $=1.38 \text{ \AA}$ ) respectively. For an ideal spinel structure T value is close to unity. It was observed that

all the investigated samples were closed to unity suggesting the spinel structure of Cu–Cr–R ferrite as prepared previously.

**Table 2** Values of ionic radius, crystallite size from XRD, particle size from FESEM, bulk density  $D_b$ , surface area from crystallite size and from FESEM (S) of Cu–Cr–R ferrite

Sample	Ionic radius (Å)	Crystallite size XRD (nm)	Particle size FESEM (µm)	$D_b$ (gm/cm <sup>3</sup> )	S Crystal size ×10 <sup>4</sup> (cm <sup>2</sup> /g)	S FESEM ×10 <sup>4</sup> (cm <sup>2</sup> /g)
CuCr	–	100	3.132	4.573	13.12	0.42
La	1.032	161.4	4.962	4.670	7.96	0.26
Ce	1.010	108.8	5.323	3.953	13.94	0.27
Nd	0.983	108.4	5.972	4.080	13.57	0.25
Sm	0.958	104.3	12.479	4.279	13.44	0.11

**Table 3** EDX analysis for Cu–Cr–R ferrite

Element	Weight percentage (wt%)		Atomic percentage (At.%)	
	Theoretical	From EDX analysis	Theoretical	from EDX analysis
<b>CuCr</b>				
Cu <sub>29</sub> K	26.691	29.42	14.286	18.65
Cr <sub>24</sub> K	6.552	7.76	4.285	6.01
Fe <sub>26</sub> K	39.876	46.08	24.286	33.23
O <sub>8</sub> K	26.88	16.73	57.143	42.12
<b>La</b>				
Cu <sub>29</sub> K	26.415	28.30	14.286	18.41
Cr <sub>24</sub> K	6.484	8.11	4.286	6.45
La <sub>57</sub> L	1.7322	3.03	0.4286	0.90
Fe <sub>26</sub> K	38.767	44.61	23.857	33.02
O <sub>8</sub> K	26.602	15.95	57.143	41.22
<b>Ce</b>				
Cu <sub>29</sub> K	26.411	26.16	14.286	16.74
Cr <sub>24</sub> K	6.483	8.11	4.286	6.34
Ce <sub>58</sub> L	1.747	2.97	0.429	0.86
Fe <sub>26</sub> K	38.761	46.01	23.857	33.50
O <sub>8</sub> K	26.598	16.75	57.143	42.56
<b>Nd</b>				
Cu <sub>29</sub> K	26.397	26.25	14.286	16.81
Cr <sub>24</sub> K	6.480	8.00	4.286	6.26
Nd <sub>60</sub> L	1.797	3.03	0.429	0.85
Fe <sub>26</sub> K	38.741	45.97	23.857	33.48
O <sub>8</sub> K	26.585	16.76	57.143	42.60
<b>Sm</b>				
Cu <sub>29</sub> K	26.377	26.95	14.286	17.67
Cr <sub>24</sub> K	6.475	8.40	4.286	6.73
Sm <sub>62</sub> L	1.872	3.99	0.429	1.11
Fe <sub>26</sub> K	38.711	44.92	23.857	33.51
O <sub>8</sub> K	26.564	15.74	57.143	40.99

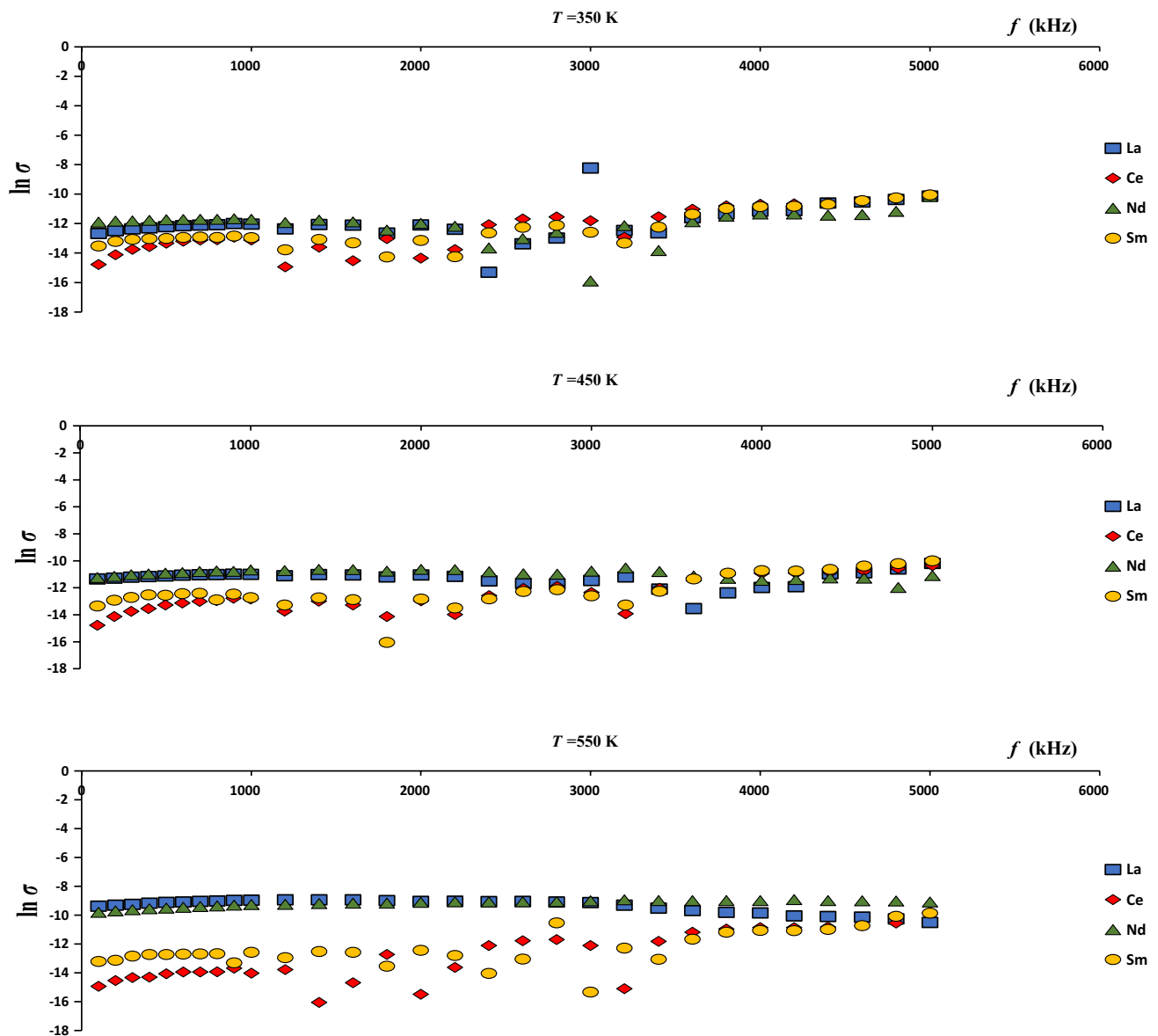
**3.1 Field emission scanning electron microscopy (FESEM) analysis**

Figure 2a showed FESEM images of CuCr<sub>0.3</sub>R<sub>0.03</sub>Fe<sub>1.67</sub>O<sub>4</sub>, (R=La, Ce, Nd and Sm). The micrographs of all samples has inhomogeneous grain size distribution. This may be due to the agglomeration of large clusters, that held together through relatively weak bonds of either magnetic or Van der Walls force [15]. The agglomeration of particles were depended on many factors such as: shape factor, surface area, porosity and density as shown in Tables 1 and 2.

The inset of Fig. 2b showed the Histogram of the average particle size measured by Image J manufactured from NIH Image company and are tabulated in Table 2. From this table, the particle size decrease by increasing ionic radius of R ions from 12 to 3 µm. This might be attributed to the ionic radius of R ions in which some of R ions might reside on the grain boundaries and inhibited the grain growth and also exert stress on the grain which caused decreasing in the particle size [16]. Table 2 showed the crystallite size calculated from XRD analysis and the particle size calculated from FESEM analysis. It was observed that the particle size from FESEM greater than that from XRD analysis due to the fact that XRD analysis gave the information of crystalline region only but the contribution from amorphous grain surface did not considered. On the other hand, FESEM gave the overall image of the particles. Also calculated specific surface area (S) from XRD analysis and from FESEM analysis were calculated using the following relation [17]:

$$S = \frac{6000}{\text{Partical size} \times \text{bulk density}} \tag{6}$$

It was observed from the calculation that the specific surface area increased as the particle size decreased.



**Fig. 3** The AC conductivity of Cu–Cr–R ferrite

### 3.2 Energy dispersion X-ray analysis (EDX) analysis

Figure 2b and Table 3 showed the compositional analysis for  $\text{CuCr}_{0.3}\text{R}_{0.03}\text{Fe}_{1.67}\text{O}_4$  ( $\text{R}=\text{La}, \text{Ce}, \text{Nd}$  and  $\text{Sm}$ ). The figure and the table showed the elemental percentage of each element which were expected to be present in the finally sintered samples. The detail of composition of different R ions samples were listed in Table 3. The energy of K, L and M series X-rays increased by increasing the atomic number. The light elements could emit X-rays of L or K-series and L-series in the normal energy range which is typical for most spectrometers, (15–20 kV). Intermediate elements could emit X-rays of L or K-series and L series. On

contrast heavy elements could emit X-ray of M or L-series and M-series [18]. As a result, a wide range of elements might be recorded simultaneously during FESEM analysis. In the investigated samples  $\text{CuCr}_{0.3}\text{Fe}_{1.7}\text{O}_4$  had light elements. By adding R elements it became heavy elements. Table 3 showed the atomic percentage (At.%) and weight percentage (wt%) for the investigated samples calculated theoretically and from EDX analysis. It was observed that the stoichiometry is nearly closed to anticipated values with small deficiencies. Finally, the incorporation of  $\text{R}^{3+}$  ions in place of  $\text{Fe}^{3+}$  was indicated by the intensities of the respective peaks in EDX analysis.

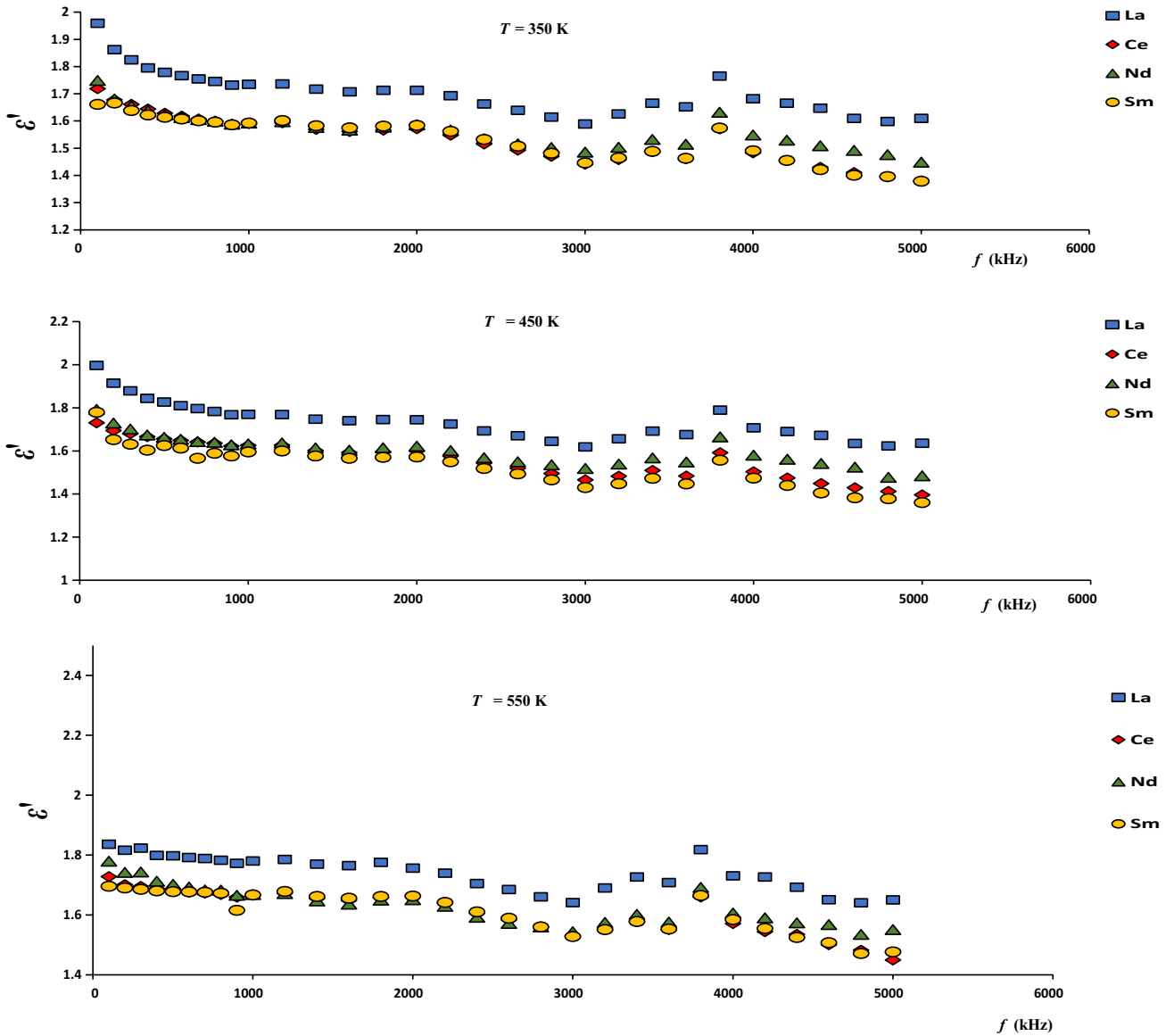


Fig. 4 The dielectric constant of Cu–Cr–R ferrite

### 3.3 Electrical properties

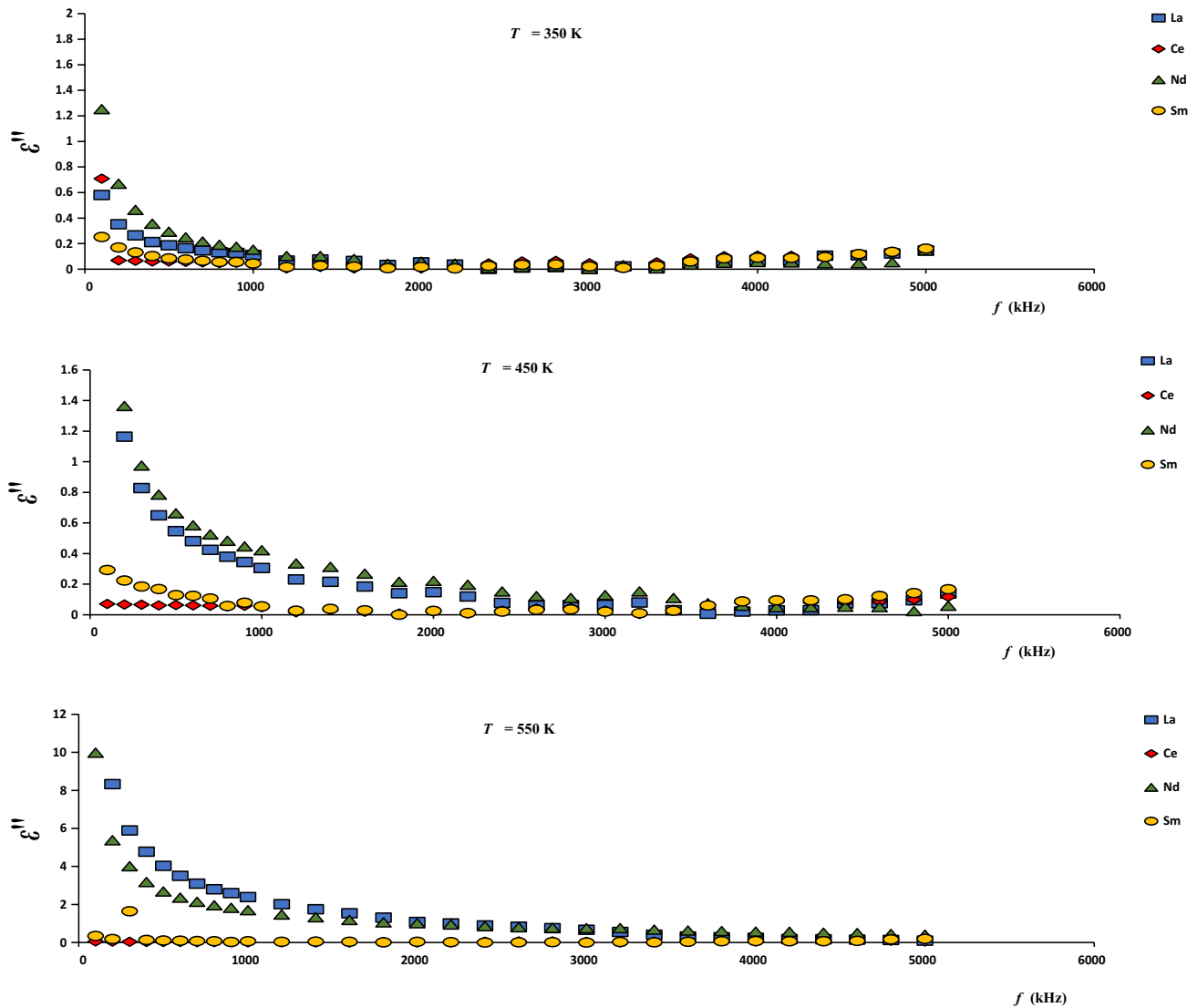
#### 3.3.1 Electrical conductivity

Figure 3 showed the variation of AC conductivity against the frequency for  $\text{CuCr}_{0.3}\text{R}_{0.03}\text{Fe}_{1.67}\text{O}_4$ ; R = Sm, Nd, Ce and La. It was noticed that  $\sigma_{ac}$  remains almost constant in relatively low frequency region then it increased in higher frequency region. As the frequency of the applied electric field increased, the hopping of charge carriers between the ions of  $\text{Fe}^{2+} \leftrightarrow \text{Fe}^{3+}$  and  $\text{R}^{3+} \leftrightarrow \text{R}^{2+}$  increased, thereby the conduction of such ferrite increased. This type of behavior showed that more than one activation barriers

with different activation energies existed. The results could be explained in terms of two regions depending on the applied frequency; region I (100 kHz–1 MHz) and region II (1–5 MHz). In region I the conduction was due to the resistive grain boundaries. While as in region II might be due to some trapped energy states, by promoting the hopping between the different charge carriers located at B-site [19].

The linearity of  $\sigma_{ac}$  frequency dependence, in region II was attributed to small polaron type conduction [20]. In general the total conductivity can be expressed as [21]:

$$\sigma_{total} = \sigma_{dc} + \sigma_{ac} \tag{7}$$



**Fig. 5** The dielectric loss of Cu–Cr–R ferrite

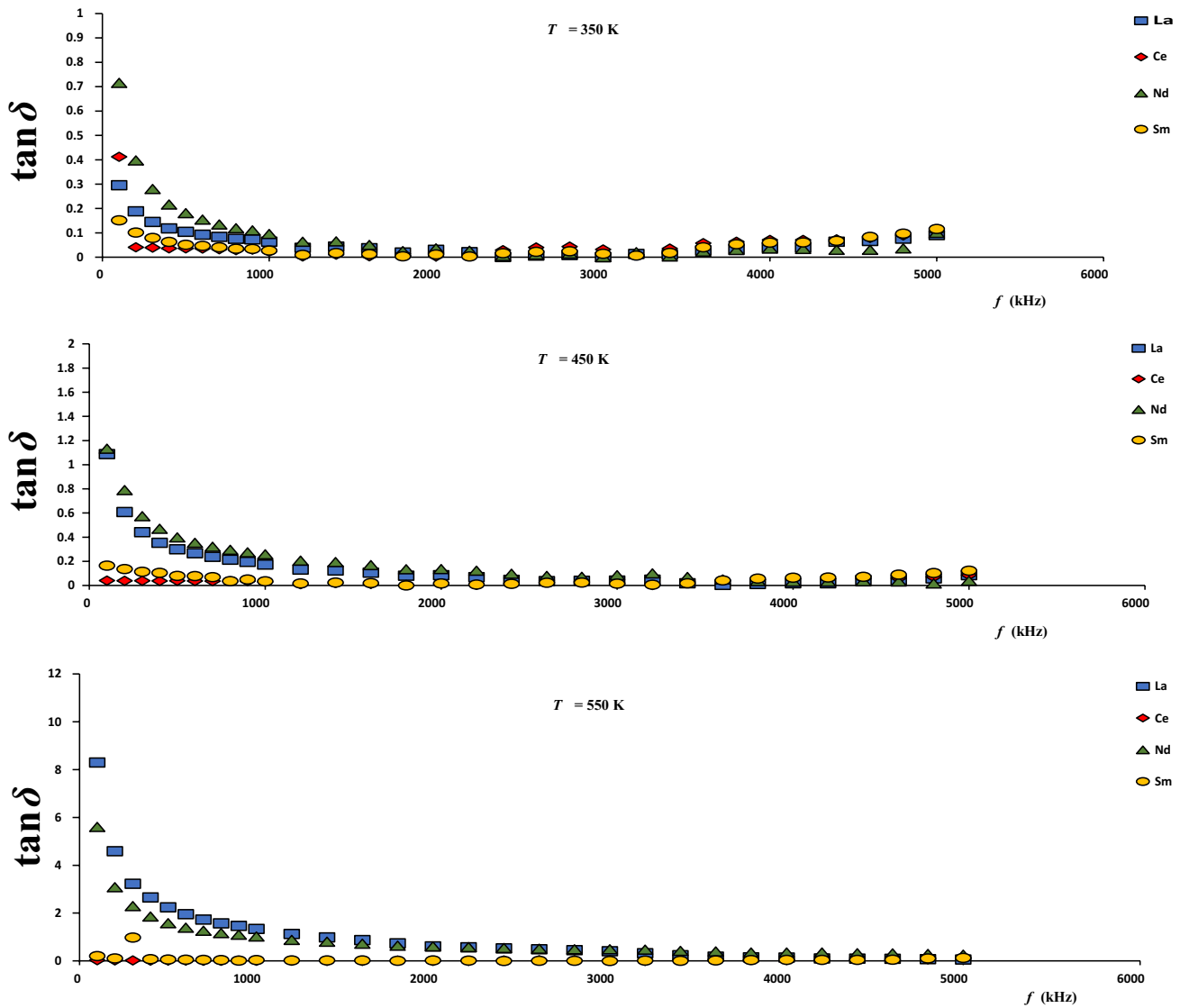
where  $\sigma_{dc}$  is the direct current conductivity which is related to the dielectric relaxation of the bounded charge carriers and  $\sigma_{ac}$  is the alternating current conductivity. The second term in Eq. (7),  $\sigma_{ac}$ , is a frequency and temperature dependent and it is predominant at high frequencies at low temperatures.

Figure 3 showed the effect of rare-earth type on the AC conductivity at different temperatures (350, 450 and 550 K) and different frequencies. Ce-doped sample had the highest electrical conductivity among this group. While, Sm doped sample had the lowest AC conductivity. The results could be interpreted on the basis of ionic radius, electronic configuration of the different rare earth elements used as well as the ionization potential of the rare element.

### 3.4 Dielectric properties

Figures 4, 5 showed the frequency dependence of the real part ( $\epsilon'$ ) and imaginary part ( $\epsilon''$ ) respectively for all investigated samples at different temperatures (350, 450, 550 K), for  $\text{CuCr}_{0.3}\text{R}_{0.03}\text{Fe}_{1.67}\text{O}_4$  samples, the dielectric constant ( $\epsilon'$ ) and dielectric loss ( $\epsilon''$ ) decreased with increasing frequency. By adding R ions with larger ionic radii, the dielectric constant ( $\epsilon'$ ) increased. The dispersion in both dielectric constant ( $\epsilon'$ ) and dielectric loss ( $\epsilon''$ ) were rapid at lower frequency range ( $10^5$ – $10^6$  Hz) which were due to interfacial polarization. At higher frequency range, due to rotational displacements of the dipoles which results in the orientational polarization, dispersion in dielectric constant ( $\epsilon'$ ) and dielectric loss ( $\epsilon''$ ) become small approaches a nearly frequency independent response





**Fig. 6** The dielectric loss tangent of Cu–Cr–R ferrite

[21]. The dielectric constant ( $\epsilon'$ ) and dielectric loss ( $\epsilon''$ ) could be described by the following relations [22].

$$\epsilon' = \epsilon_{\infty} + \frac{\epsilon_s - \epsilon_{\infty}}{1 + \omega^2 \tau^2} \tag{8}$$

$$\epsilon'' = \frac{(\epsilon_s - \epsilon_{\infty})\omega\tau}{1 + \omega^2 \tau^2} \tag{9}$$

$$\tan \delta = \frac{\epsilon''}{\epsilon'} \tag{10}$$

where  $\epsilon_s$  is the static dielectric constant,  $\epsilon_{\infty}$  is high frequency limit of dielectric constant,  $\omega$  the applied angular frequency ( $2\pi f$ ),  $\tau$  the relaxation time and  $\tan \delta$  is the dielectric loss tangent. The dielectric dispersion depended

on two factors: the first was due to the electron hopping between  $\text{Fe}^{2+}$  and  $\text{Fe}^{3+}$  ions and the second was due to the space charge polarization of an inhomogeneous dielectric structure. Koop's [23] theory suggested that the sample having heterogeneous structure contains well conducting grains separated by highly resistive thin grain boundaries. This caused localized accumulation of charge under the applied electric field which built up space charge polarization. Also, from the figure the dielectric constant ( $\epsilon'$ ) and dielectric loss ( $\epsilon''$ ) increased with the increase in temperature due to thermally energized electrons, which contribute to the polarizability at higher frequency.

Figure 6 showed the dielectric loss tangent, which decreased with increasing frequency and this is normal dielectric behavior in ferrites. It was noticed that the Ce

sample has the lowest dielectric constant values and dielectric loss factor. The variation of dielectric loss tangent ( $\tan\delta$ ) with increasing frequency showed the same trend similar to that of dielectric constant ( $\epsilon'$ ) and dielectric loss ( $\epsilon''$ ). The decrease was rapid at lower frequencies and became slower at higher frequencies, where the electrons were localized at the grain boundary through hopping produced polarization. As the frequency of the applied field was increased, the electrons reversed their direction of motion more often.

In general, the temperature dependence behavior of dielectric constant ( $\epsilon'$ ) and dielectric loss ( $\epsilon''$ ) and  $\tan\delta$  could be explained as follows: dielectric constant in ferrites was attributed to four types of polarization: interfacial ( $P_1$ ), dipolar ( $P_d$ ), electronic ( $P_e$ ) and space charge ( $P_{sc}$ ). At low frequencies where all four types of polarization contribute, the rapid increase in ( $\epsilon'$ ) and ( $\epsilon''$ ) with temperature were mainly due to interfacial and dipolar polarization, which were strongly temperature dependent [24]. In case of the interfacial polarization, which was due to the accumulation of charges at the grain boundary, an increase in polarization results more charges reached the grain boundary as temperature increased. The decrease of ( $\epsilon'$ ) and ( $\epsilon''$ ) beyond the temperature at which the last maximum appeared, was attributed to the decrease in internal viscosity of the system giving rise to more degrees of freedom to the dipoles which results in increasing the disordering of the system and hence decreasing both ( $\epsilon'$ ) and ( $\epsilon''$ ) again.

Dielectric loss tangent was an important part of the total core loss in ferrites. Hence, for low core loss, low dielectric loss is desirable. Dielectric loss ( $\tan\delta$ ) represented the energy of dissipation in the dielectric system. The hopping (exchange) of the charge carriers in the octahedral sites (which was responsible for electric conduction) was thermally activated by an increase in temperature. As a result, the dielectric polarization increased causing an increase in  $\epsilon'$ ,  $\epsilon''$  and  $\tan\delta$ . Therefore,  $\epsilon'$ ,  $\epsilon''$  and  $\tan\delta$  increased with the temperature and decreased with frequency which is a normal behavior for semiconducting ferrites.

Finally, addition of R ions gave highest conduction as follow:  $Ce > Nd > Sm > La$  and gave the dielectric loss as follow:  $Nd > La > Sm > Ce$ . This means that  $CuCr_{0.3}La_{0.03}Fe_{1.67}O_4$  ferrite had the highest resistivity which is the preferable sample in many technological applications.

## 4 Conclusion

1. X-ray analysis confirmed that all samples had were face centered cubic (fcc) structure single phase spinel structure with small secondary phase peaks.

2. FESEM analyses explained the morphology of the particles. The micrographs of all samples had inhomogeneous grain size distribution. The particles showed irregular shapes by adding different R ions.
3. EDX data gives the elemental % and atomic % in the composition of mixed Cu–Cr–R ferrites, and it shows the presence of all cations of the samples.
4. The most recommendable sample satisfies the technological application is  $CuCr_{0.3}La_{0.03}Fe_{1.67}O_4$  which has higher resistivity, low crystallite size and valence stability potential promising application in memories and microelectronics.

## References

1. M.J. Iqbal, Z. Ahmad, Y. Melikhov, I.C. Nlebedim, J. Magn. Mater. **324**, 1088 (2012)
2. M.A. Rahman, M.A. Rahman, A.K.M.A. Hossain, J. Magn. Mater. **369**, 168 (2014)
3. X. Zhou, J. Jiang, L. Li, F. Xu, J. Magn. Mater. **314**, 7 (2007)
4. A. Ashok, T. Somaiah, D. Ravinder, C. Venkateshwarlu, C.S. Reddy, K.N. Rao, M. Prasad, World J. Condens. Matter. Phys. **2**, 257–266 (2012)
5. W. Ling, H. Zhang, Y. He, Y. Li, Y. Wang, Prog. Nat. Sci. Mater. Int. **21**, 21–26 (2011)
6. S. Kimura, T. Mashino, T. Hiroki, D. Shigeoka, N. Sakai, L. Zhu, Y. Ichiyangi, Thermochim. Acta **532**, 119 (2012)
7. C. Venkataraju, G. Sathishkumar, K. Sivakumar, J. Magn. Mater. **322**, 230 (2010)
8. Y.M.Z. Ahmed, Ceram. Int. **36**, 969 (2010)
9. Z. Wang, L. Xiao, R. Liang, S. Shen, J. Xu, J. Wang, AIP Adv. **6**, 65221 (2016)
10. D.R. Mane, D.D. Birajdar, S. Patil, S.E. Shirsath, R.H. Kadam, J. Sol–Gel Sci. Technol. **58**, 70 (2010)
11. R.D. Shannon, Acta Crystallogr. Sect. A **32**, 751 (1976)
12. P.K. Roy, B.B. Nayak, J. Bera, J. Magn. Mater. **320**, 1128 (2008)
13. Y.L.N. Murthy, T. Kondala Rao, I.V. Kasi Viswanath, R. Singh, J. Magn. Mater. **322**, 2071 (2010)
14. K.K. Bamzai, G. Kour, B. Kaur, S.D. Kulkarni, J. Magn. Mater. **327**, 159 (2013)
15. D. Xiong, Q. Zhang, S.K. Verma, H. Li, W. Chen, X. Zhao, J. Alloys Compd. **662**, 374 (2016)
16. S. Modak, M. Ammar, F. Mazaleyrat, S. Das, P.K. Chakrabarti, J. Alloys Compd. **473**, 15 (2009)
17. D. Xiong, Q. Zhang, Z. Du, S.K. Verma, H. Li, X. Zhao, New J. Chem. **40**, 6498 (2016)
18. R. Tholkappiyian, K. Vishista, Phys. B Condens Matter **448**, 177 (2014)
19. D. Ravinder, P. Vijaya Bhasker Reddy, Mater. Lett. **57**, 4344 (2003)
20. K. Iwauchi, Jpn. J. Appl. Phys. **10**, 1520 (1971)
21. A.M. Abdeen, O.M. Hemeda, E.E. Assem, M.M. El-Sehly, J. Magn. Mater. **238**, 75 (2002)
22. S.D. Shenoy, P.A. Joy, M.R. Anantharaman, J. Magn. Mater. **269**, 217 (2004)
23. C.G. Koops, Phys. Rev. **83**, 121 (1951)
24. M.A. Ahmed, A.A. Azab, E.H. El-Khawas, J. Mater. Sci. Mater. Electron **26**, 8765 (2015)